Journal of Magnetic Resonance 213 (2011) 126–135

Contents lists available at SciVerse ScienceDirect

Journal of Magnetic Resonance

journal homepage: www.elsevier.com/locate/jmr

Robust slice-selective broadband refocusing pulses

Martin A. Janich [a,b,c], Rolf F. Schulte [b], Markus Schwaiger [c], Steffen J. Glaser [a,*]

[a] Technische Universität München, Department of Chemistry, Munich, Germany
[b] GE Global Research, Munich, Germany
[c] Technische Universität München, Nuclear Medicine, Munich, Germany

ARTICLE INFO

Article history:
Received 11 July 2011
Revised 6 September 2011
Available online 16 September 2011

Keywords:
Magnetic resonance spectroscopy
Radiofrequency pulse
Broadband refocusing
Optimal control theory
PRESS
BURBOP

ABSTRACT

Slice-selective broadband refocusing pulses are of great interest in localized MR spectroscopy for improving spatial selectivity, reducing chemical-shift displacement errors, and reducing anomalous J modulation. In practice the bandwidth of RF pulses is limited by the maximum available B_1 amplitude. The goal of the present work is to design slice-selective and broadband refocusing pulses which are tolerant against B_1 deviations. Pulse design is performed by numerical optimization based on optimal control theory. A comprehensive study of different cost functions and their effect on the optimization is given.

The optimized slice-selective broadband refocusing pulses are compared to conventional Shinnar-Le Roux (SLR), broadband SLR, and hyperbolic secant pulses. In simulations and experiments optimized pulses were shown to fulfill broadband slice specifications over a range of ±20% B_1 scalings. Experimental validation showed a reduction of chemical-shift displacement error by a factor of 3 compared to conventional SLR pulses.

© 2011 Elsevier Inc. All rights reserved.

1. Introduction

Magnetic resonance spectroscopy enables non-invasive measurements of metabolite concentrations, making it a powerful tool for numerous pathologic conditions, including epilepsy, multiple sclerosis, stroke, cancer, and metabolic disorders [1]. For in vivo measurements good localization is crucial in order to obtain meaningful signals with narrow line widths. In brain spectroscopy unwanted strong signals from a lipid layer beside the skull are usually reduced by repeatedly applying outer volume suppression. This can be omitted or reduced with improved localization. For localization with point resolved spectroscopy (PRESS) [2] a spin-echo is generated from within a cuboidal voxel by an excitation pulse and two refocusing pulses combined with three slice selection gradients applied along orthogonal axes. PRESS can be used for single-voxel spectroscopy and chemical-shift imaging (CSI) [3].

Typical problems of PRESS are poor selectivity profiles, chemical-shift displacement errors (CSDE), and spatially dependent evolution of J-coupling within the voxel. These errors can be reduced with larger RF pulse bandwidth [4,5]. In experiments the RF pulse bandwidth is limited because of the maximum available RF amplitude ($B_{1,max}$) which is constrained by hardware and energy deposition (SAR). The relative displacement of water and fat for a typical pulse bandwidth of BW = 1 kHz at B_0 = 3 T is 45% of slice thickness.

Refocusing pulses are not only needed for generating spin echoes as in the PRESS sequence but also in other contexts of magnetic resonance spectroscopy, for example polarization transfer and spectral editing. This class of pulses is commonly called spin-echo [6,7], refocusing [8], or universal rotation (UR) [9].

The RF pulse bandwidth under given $B_{1,max}$ constraints can be increased by reducing the flip angle, e.g. from 180° to 163° [10]. This however decreases the signal and therefore it is desired to obtain both a large bandwidth and a 180° flip angle.

The bandwidth and selectivity of refocusing pulses can be increased by allowing phase modulation, which makes it possible to spread the pulse energy over a larger region of the pulse shape and therefore decreasing $B_{1,max}$. Previously, the Shinnar-Le Roux transformation (SLR) [7] was used to design broadband refocusing pulses [8]. This design alters the pulse phase by flipping of zeros of the SLR A-polynomial while preserving the refocusing profile [11,12]. Large bandwidth is obtained by non-linear optimization of the zero-flipping pattern. With the SLR algorithm only flip-angles below 180° can be obtained, leading to a signal reduction compared to 180° flip angles. The major drawback of broadband (BB) SLR pulses is their large sensitivity to B_1 scaling with increased bandwidth. This may prevent their experimental applicability due to spatially inhomogeneous B_1 fields and B_1 calibration errors.

High robustness against B_1 scaling can be reached with adiabatic frequency-swept pulses. However, these pulses are inversion pulses and not refocusing pulses. For spin refocusing they need to be used in pairs, in a double spin-echo sequence [13]. Localization by adiabatic

* Corresponding author. Address: Department of Chemistry, Technische Universität München, Lichtenbergstr. 4, 85747 Garching, Germany.
E-mail address: Glaser@tum.de (S.J. Glaser).

1090-7807/$ - see front matter © 2011 Elsevier Inc. All rights reserved.
doi:10.1016/j.jmr.2011.09.025

selective refocusing (LASER) uses broadband and B_1-insensitive pulses, but it is not applicable to short echo times [14].

The above mentioned difficulties of existing refocusing pulses can be addressed using optimal control theory. With this flexible RF pulse design a tradeoff can be made between bandwidth under given $B_{1,\max}$ constraints, robustness against B_1 scaling, pulse duration, and error in the magnetization profile (ripple). Numerical tools based on optimal control theory have been developed for the design of slice-selective [6,15–17] and broadband pulses [18–22] for single spins, and coupled spin systems [23–26]. Optimal control theory was also applied to non-selective, broadband, B_1 - robust refocusing [9,27,28].

The goal of the present work is to optimize slice-selective, broadband refocusing pulses which are robust against B_1 scaling. Our pulses are called "Slice-selective Broadband Universal Rotation By Optimized Pulses" (S-BURBOP). They are compared to conventional SLR, broadband (BB) SLR, and a pair of adiabatic frequency-swept pulses, and are applied and experimentally validated in PRESS experiments.

2. Theory and methods

2.1. RF pulse optimization

Slice-selective refocusing pulses were designed using numerical algorithms based on optimal control theory. The underlying optimization principle is that if a control variable $\omega_{1,j} = \omega_{1,x,j} + i\omega_{1,y,j}$, $j = 1,\ldots,N$ is optimal, then a small perturbation $\delta\omega_{1,j}$ will cause no change to the cost function Φ. The stationary condition $\delta\Phi/\delta\omega_{1,j} \stackrel{!}{=} 0$ is the first-order necessary condition for an optimal RF pulse $\omega_{1,j}$. The physical and practical constraints are the maximum pulse duration, given by the desired echo time, and the maximum available RF amplitude ($B_{1,\max}$).

The RF pulse is optimized iteratively with the following gradient search method, adapted from [18,23]:

1. Choose initial pulse $\omega_{1,j} j = 1,\ldots,N$
2. Calculate first-order gradient $\delta\Phi/\delta\omega_{1,j}$
3. Update RF pulse according to $\omega_{1,j} \rightarrow \omega_{1,j} + \epsilon\delta\Phi/\delta\omega_{1,j}$
4. Apply low-pass filter to $\omega_{1,j}$
5. Truncate $\omega_{1,j}$ at $B_{1,\max}$
6. Repeat steps 2–5 until termination condition is reached

The step size ϵ for adding the first-order gradient to the pulse is calculated by line search [29]. The reason for low-pass filtering is described in Section 2.4.

The cost function for S-BURBOP combines the cost functions for universal rotation (UR) and point-to-point transformation (PP). In the pass-band refocusing characteristics are obtained by optimizing 180° UR and in the stop-band excitation is prevented by mapping thermal equilibrium magnetization to itself using PP (see Section 2.4). The goal of PP optimization is to find the trajectory for the initial magnetization vector $\vec{M}_0$ that optimizes a suitably chosen cost function. On the other hand, UR optimization aims at rotation of any magnetization vector by a desired rotation angle around a desired rotation axis. The evolution for PP and UR, corresponding costs and gradients are described in the following two sections.

2.2. Point-to-point transformations

The Bloch equation for a time-varying and piecewise constant RF field

$$B_{1,j} = B_{1,x,j} + iB_{1,y,j}, \quad j = 1,\ldots,N \tag{1}$$

of duration $T = N \cdot \Delta t$, neglecting relaxation, is given by [7]

$$\begin{bmatrix} \dot{M}_{x,j} \\ \dot{M}_{y,j} \\ \dot{M}_{z,j} \end{bmatrix} = \begin{bmatrix} 0 & \gamma G_x x & -\gamma B_{1,y,j} \\ -\gamma G_x x & 0 & \gamma B_{1,x,j} \\ \gamma B_{1,y,j} & -\gamma B_{1,x,j} & 0 \end{bmatrix} \begin{bmatrix} M_{x,j} \\ M_{y,j} \\ M_{z,j} \end{bmatrix} \tag{2}$$

The frequency $\Delta\omega = -\gamma G_x x$ corresponds to a spatial location x when the RF pulse is applied simultaneously with a magnetic field gradient $G_x = \delta B_z/\delta x$. A different expression of the Bloch equation is given by

$$\dot{\vec{M}}_j = \vec{\omega}_j \times \vec{M}_j \tag{3}$$

with the magnetization vector $\vec{M}_j = [M_{x,j}\ M_{y,j}\ M_{z,j}]^T$ and the effective rotation $\vec{\omega}_j = [-\gamma B_{1,x,j}\ -\gamma B_{1,y,j}\ -\gamma G_x x]^T$.

The propagation of a magnetization vector $\vec{M}_0$ is executed by a sequence of 3×3 rotation matrices

$$\vec{M}_N = R_N \cdot R_{N-1} \cdots R_j \cdots R_1 \cdot \vec{M}_0 \tag{4}$$

with rotation axis

$$\vec{n}_j = \frac{\vec{\omega}_j}{|\vec{\omega}_j|} \tag{5}$$

and rotation angle

$$\phi_j = \Delta t|\vec{\omega}_j| \tag{6}$$

The iterative optimization algorithm for PP transformation of an initial magnetization vector $\vec{M}_0$ to a desired final magnetization vector $\vec{M}_t$ is explained in detail by Skinner et al. [18]. The cost function to be minimized reflects the projection of the actual final magnetization vector on the desired magnetization vector

$$\Phi_{\text{pp}}(\vec{M}_0, \vec{M}_t) := 0.5 - 0.5\left(\vec{M}_t^T \vec{M}_N\right), \Phi_{\text{pp}} \in [0, 1] \tag{7}$$

A decreasing cost Φ_{pp} quantifies the degree to which the magnetization vector $\vec{M}_N$ after application of the RF pulse becomes the target magnetization vector $\vec{M}_t$.

The necessary condition that must be satisfied at each time for Φ_{pp} to be minimized is

$$\vec{g}_j := \frac{\delta\Phi_{\text{pp}}}{\delta\vec{\omega}_j} = 0 \tag{8}$$

The first-order derivative of the cost function is obtained by back-propagation of $\vec{M}_N \times \vec{M}_t$:

$$\begin{aligned} \vec{g}_N &= \vec{M}_N \times \vec{M}_t \\ \dot{\vec{g}}_j &= \vec{\omega}_j \times \vec{g}_j \end{aligned} \tag{9}$$

2.3. Universal rotations

The obtained RF pulse from PP optimization is only defined for transforming $\vec{M}_0$ to $\vec{M}_t$ and not for any other vector. The rotation of any given magnetization vector by a desired angle ϕ_t and rotation axis $\vec{n}_t$ is called universal rotation (UR). Here, we adapt the spinor notation [7].

A desired universal rotation can be described by the 2×2 unitary matrix

$$Q_t = \begin{bmatrix} \alpha_t & -\beta_t^* \\ \beta_t & \alpha_t^* \end{bmatrix} \tag{10}$$

with the Cayley-Klein parameters

$$\alpha_t = \cos\frac{\phi_t}{2} - \mathrm{i}n_{z,t}\sin\frac{\phi_t}{2}$$
$$\beta_t = (n_{y,t} - \mathrm{i}n_{x,t})\sin\frac{\phi_t}{2} \quad (11)$$
$$1 = \alpha_t\alpha_t^* + \beta_t\beta_t^*$$

With the piecewise constant RF pulse $B_{1,j}$ (Eq. (1)) the resulting UR can be described by a sequence of unitary matrices

$$Q = Q_N \cdot Q_{N-1} \cdots Q_j \cdots Q_1 \quad (12)$$

with

$$Q_j = \begin{bmatrix} a_j & -b_j^* \\ b_j & a_j^* \end{bmatrix} \quad (13)$$

The Cayley-Klein parameters a_j and b_j for the pulse interval j are defined as in Eq. (11).

The propagation in state-space description of universal rotations is given by

$$\begin{bmatrix} \alpha_j \\ \beta_j \end{bmatrix} = \begin{bmatrix} a_j & -b_j^* \\ b_j & a_j^* \end{bmatrix} \begin{bmatrix} \alpha_{j-1} \\ \beta_{j-1} \end{bmatrix} \quad (14)$$

with the initial state being

$$\begin{bmatrix} \alpha_0 \\ \beta_0 \end{bmatrix} = \begin{bmatrix} 1 \\ 0 \end{bmatrix} \quad (15)$$

Pulse optimization minimizes the cost function

$$\Phi_{\mathrm{ur}} := 0.5 - 0.25\mathrm{tr}\left\{Q_t^\dagger \cdot Q\right\},\ \Phi_{\mathrm{ur}} \in [0,1] \quad (16)$$

where † stands for the conjugate transpose and tr sums the matrix elements on the main diagonal. This maximizes the projection of the final rotation matrix Q on the target rotation Q_t. Note that $\mathrm{tr}\left\{Q_t^\dagger \cdot Q\right\} \in \mathbb{R}$. Due to the 4π-periodicity of quantum mechanical rotations of spin 1/2 particles, this quality factor makes it possible to distinguish π rotation around the x vs. $-x$ axis (or π vs. $-\pi$ rotation around the x axis; see Appendix A).

The first-order derivative for universal rotations was derived previously for coupled spin systems [23,27]. The time-evolution of the spin system during a time step j is given by the propagator

$$Q_j = \exp\{-\mathrm{i}\Delta t(H_0 + \omega_{1,x,j}H_x + \omega_{1,y,j}H_y)\} \quad (17)$$

with the free evolution Hamiltonian H_0 and the RF Hamiltonians

$$H_x = \frac{1}{2}\begin{bmatrix} 0 & 1 \\ 1 & 0 \end{bmatrix} \text{ and } H_y = \frac{1}{2\mathrm{i}}\begin{bmatrix} 0 & 1 \\ -1 & 0 \end{bmatrix} \quad (18)$$

For single spins the first-order derivative is

$$\frac{\delta\Phi_{\mathrm{ur}}}{\delta\omega_{1,x,j}} = -0.25\mathrm{tr}\left\{Q_t^\dagger \cdot Q_N \cdot Q_{N-1} \cdots Q_{j+1} \cdot (-\mathrm{i}\Delta t H_x) \cdot Q_j \cdots Q_1\right\} \quad (19)$$

and correspondingly for the derivative with respect to $\omega_{1,y,j}$. The gradient can be efficiently calculated by saving the results of the forward-propagation $R_j = Q_j \cdots Q_1$ and of the backward-propagation $S_j = Q_t^\dagger \cdot Q_N \cdot Q_{N-1} \cdots Q_{j+1}$ for each time step j. Then the x-gradient is obtained with

$$\frac{\delta\Phi_{\mathrm{ur}}}{\delta\omega_{1,x,j}} = 0.25\mathrm{i}\Delta t(\mathrm{tr}\{S_j \cdot H_x \cdot R_j\}) \quad (20)$$

and correspondingly for the y-gradient. Note that the gradient consists of real numbers.

The quality factor Φ_{ur} (Eq. (16)) based on $\mathrm{tr}\left\{Q_t^\dagger \cdot Q\right\}$ is sensitive to the global phase of Q and hence can distinguish e.g. π from $-\pi$ rotations around the x-axis. As pointed out in Ref. [23] the global phase of Q has no experimental significance, which can be expressed by an alternative quality factor based on $\left|\mathrm{tr}\left\{Q_t^\dagger \cdot Q\right\}\right|^2$:

$$\Phi_{\mathrm{ur2}} := 1 - 0.25\left|\mathrm{tr}\left\{Q_t^\dagger \cdot Q\right\}\right|^2,\ \Phi_{\mathrm{ur2}} \in [0,1] \quad (21)$$

As shown in Appendix A this quality factor based on the unitary matrix Q is identical to the quality factor

$$\Phi_{xyz} := 0.5\left[\Phi_{\mathrm{pp}}(\vec{M}_{0,1}, \vec{M}_{t,1}) + \Phi_{\mathrm{pp}}(\vec{M}_{0,2}, \vec{M}_{t,2}) + \Phi_{\mathrm{pp}}(\vec{M}_{0,3}, \vec{M}_{t,3})\right] \quad (22)$$

which is based on the properties of three independent PP transformations for the three initial magnetization vectors $\vec{M}_{0,1}$, $\vec{M}_{0,2}$, $\vec{M}_{0,3}$, which are orthogonal to each other, and the target vectors

$$\vec{M}_{t,1} = R_t\vec{M}_{0,1},\ \vec{M}_{t,2} = R_t\vec{M}_{0,2},\ \vec{M}_{t,3} = R_t\vec{M}_{0,3} \quad (23)$$

representing the initial vectors rotated by ϕ_t around axis $\vec{n}_t$, where R_t is the desired rotation matrix (see Appendix A). This cost function has the advantage of using only PP transformations and therefore being more straightforward to implement.

The cost function $\Phi_{xyz} = \Phi_{\mathrm{ur2}}$ has a 2 π-periodicity and therefore π rotations around the x vs. $-x$ axis cannot be distinguished (or π vs. $-\pi$ rotations around the x axis). This is in contrast to Φ_{ur} which makes this distinction. The periodicity of Φ_{ur} and $\Phi_{xyz} = \Phi_{\mathrm{ur2}}$ and the resulting sensitivity toward positive or negative direction of π rotations are discussed in Table 1 and Appendix A.

2.4. Cost function for S-BURBOP

The goal of pulse optimization is to create an RF pulse with a desired performance for different off-resonance frequencies and B_1 scalings. This is obtained by averaging over several cost functions and gradients [18,23,16].

Slice-selective performance is obtained by combining UR (Eq. (16)) and PP (Eq. (7)) in a single optimization routine. In the pass-band the pulse should perform universal rotation Q_t, with rotation axis $\vec{n}_t$ and angle ϕ_t. In the transition zone the pulse behavior is undefined. Finally, in the stop-band excitation is prevented by mapping magnetization aligned along the z-axis to itself, by performing PP with $\vec{M}_0 = \vec{M}_t = [0\,0\,1]^T$. Alternatively the performance in the stop-band can be described by universal rotation around the z-axis [30]. For UR the desired rotation angle needs to be specified. This angle is caused by the effect of free precession together with a transient Bloch-Siegert shift. The approximation of the transient Bloch-Siegert shift used in reference [30] has negligible error only for large off-resonance frequencies. In contrast, using PP and mapping of z-magnetization to itself does not require the definition of a specific off-resonance dependent rotation angle around the z-axis.

The cost function for slice-selective universal rotation pulses is therefore

Table 1
The resulting transformation of magnetization vectors M_x, M_y, and M_z for a positive or negative 180° rotation around the x-axis is identical. Therefore, the cost function Φ_{xyz}, which uses this transformation, is not sensitive to the rotation direction. Φ_{xyz} equals 0 in both cases. Conversely, Φ_{ur} is sensitive to the rotation direction. It is 0 if axis, angle, and direction of the actual rotation are equal to the target rotation (in this case $180_x°$). Φ_{ur} equals 1 if the actual rotation direction is opposite to the target rotation direction.

$180_x°$	$-180_x°$
$M_x \to M_x$	$M_x \to M_x$
$M_y \to -M_y$	$M_y \to -M_y$
$M_z \to -M_z$	$M_z \to -M_z$
$\Phi_{xyz} = 0$	$\Phi_{xyz} = 0$
$\Phi_{\mathrm{ur}} = 0$	$\Phi_{\mathrm{ur}} = 1$

$$\Phi_{\text{slice}} = \sum_{\Delta\omega_k \in P} \Phi_{\text{ur}}(\vec{n}_t, \phi_t, \Delta\omega_k) w(\Delta\omega_k) + \sum_{\Delta\omega_m \in S} \Phi_{\text{pp}}(\vec{M}_0, \vec{M}_t, \Delta\omega_m) w(\Delta\omega_m) \quad (24)$$

The sets P and S include discretely sampled off-resonance frequencies in the pass-band and stop-band, respectively. The weighting factor w is chosen in a way that off-resonance frequencies further away from the pass-band have a smaller influence on the optimization. For the bandwidth BW and a slice centered around $\Delta\omega = 0$ Hz the weighting factor is defined by

$$w'(\Delta\omega) = \exp\left\{-\left|\frac{\Delta\omega}{4\pi BW} + \frac{BW}{2}\right|\right\} + \exp\left\{-\left|\frac{\Delta\omega}{4\pi BW} - \frac{BW}{2}\right|\right\} \quad (25)$$

and it is normalized with

$$w(\Delta\omega) = \left(\sum_{\Delta\omega_k \in P \bigcup S} w'(\Delta\omega_k)\right)^{-1} w'(\Delta\omega) \quad (26)$$

in order to have a sum of unity.

Excitation of transverse magnetization far beyond the pass-band is not desired. For large frequency offsets resulting transverse magnetization is simply the Fourier transform of the B_1 pulse shape [31]. The pulse shape may not contain high-frequency components and it is therefore filtered by a low-pass which suppresses frequencies above the maximum frequency $f_{lp} = 10$ kHz. The low-pass filter is implemented as a convolution of the RF pulse shape $B_{1,j}$ ($j = 1,\ldots,N$) in time domain with the sinc function

$$g_k = \frac{\sin(2\pi k f_{lp} \Delta t)}{\pi k}, \quad k = -N,\ldots,N \quad (27)$$

and it is applied in each iteration of the optimization [32]. This procedure has two advantages: it limits the number of off-resonance frequencies that need to be considered in the stop-band ($-2\pi f_{lp},\ldots,2\pi f_{lp}$) and therefore speeds up the optimization. Second, it produces smooth pulse shapes which can easily be generated by the MR hardware.

Robustness against scaling of the B_1 amplitude is obtained by a weighted average over different scalings $|B_1| \rightarrow b_p|B_1|$. The overall cost function for slice-selective, robust refocusing pulses is given by

$$\Phi = \sum_{b_p \in B} \Phi_{\text{slice}}(b_p) w_b(b_p) \quad (28)$$

For a pulse with ±10% B_1 robustness the set B is equal to {0.9, 1.0, 1.1} and for ±20% B_1 robustness it is $B = \{0.8, 0.9, 1.0, 1.1, 1.2\}$. In order to achieve a uniform performance as a function of B_1 amplitude within the specified range of B_1 values, low B_1 values needed to be weighted stronger. The empirically found weighting factors w_b for ±10% B_1 robustness were {0.56, 0.33, 0.11} and for ±20% B_1 robustness they were {0.33, 0.27, 0.20, 0.13, 0.07}, respectively.

2.5. Terminology of selective RF pulses

Design of selective RF pulses is a tradeoff between time-bandwidth product ($T \cdot BW$), fractional transition width (FTW), pulse energy (E), and ripples in the magnetization profile (δ). As bandwidth (BW) we use the full width at half maximum of the inversion magnetization profile. The FTW is the width of the transition zone divided by BW. The dimensionless number E/E_{SLR} is the pulse energy relative to a conventional SLR pulse. It is proportional to the integral over the squared B_1 amplitude. The ripples δ_{PB} and δ_{SB} are the maximum errors in the inversion magnetization profile's pass-band and stop-band, respectively. An important measure for the broadband performance achieved under $B_{1,\max}$ limitations is $BW/f_{1,\max}$, where $f_{1,\max} = -\gamma/(2\pi)B_{1,\max}$ is the maximum available RF amplitude.

2.6. Experiments

For experimental validation S-BURBOP pulses were implemented on a Bruker 600MHz/14T Avance III spectrometer (Bruker BioSpin, Rheinstetten, Germany). The pulses were scaled to $B_{1,\max} = 235$ μT which corresponds to $f_{1,\max} = 10$ kHz for ^{1}H. Magnetization slice profiles of crushed spin-echo were measured in a water sample for different B_1 scalings ($TR = 1.1$ s, $TE = 5$ ms). The pulse sequence consisted of a non-selective 90° excitation pulse followed by a slice-selective 180° refocusing pulse, which was surrounded by crusher gradients, and recording of a spin-echo. The refocusing profile obtained from this measurement was normalized to the profile obtained from a measurement omitting the refocusing pulse in order to correct for flip angle deviations of the excitation pulse.

Imaging experiments were carried out on a GE Signa HDx 3T MRI system (GE Healthcare, Milwaukee, WI, USA) using a transmit-receive head coil with $B_{1,\max} = 23$ μT. Imaging of the ^{1}H PRESS CSI voxel was performed on a phantom filled with vegetable oil and water. A $(2\text{ cm})^3$ voxel was measured with $TR = 4$ s and $TE = 50$ ms.

3. Results and discussion

3.1. Convergence of pulse optimization

The convergence of S-BURBOP pulse optimization is examined by checking the final costs starting from a large number of random initial pulses. Convergence properties of optimizations based on the cost functions Φ_{ur} (Eq. (16)) and $\Phi_{xyz} = \Phi_{\text{ur2}}$ (Eqs. (22) and (21)) are compared. Slice-selective 180_x° pulses with $T \cdot BW = 18$, $FTW = 0.1$, $BW/f_{1,\max} = 3$ are optimized without B_1 robustness with cost functions Φ_{ur} and Φ_{xyz}. The optimizations are initialized with the same 1000 random pulses and are terminated under the same conditions (maximum 1000 iterations or cost difference of two subsequent iterations below 10^{-7}).

The histograms in Fig. 1a and b show the number of pulses that end up with a specified final cost Φ_{xyz}. The cost function Φ_{xyz} is used, as it is insensitive to the rotation direction and therefore the best pulse under Φ_{ur} is also the best pulse under Φ_{xyz} (but not vice versa). The histograms show that the final costs optimized with Φ_{ur} are accumulated closer to each other and reach better costs. Therefore the fidelity of optimizations with Φ_{ur} is higher than with Φ_{xyz}.

Although the global phase of a unitary propagator Q has no physical significance in any experiment, it plays an important role in the optimization of RF pulses. This surprising fact was first discussed in the context of pulse optimizations for coupled spin systems [33] and was further studied in broadband single spin optimizations [27].

The poor fidelity using the cost function Φ_{xyz} is a result of the missing sensitivity toward rotation direction (Table 1). Fig. 1c and d shows the cost at different off-resonance frequencies for the best pulse from the Φ_{xyz} and Φ_{ur} optimizations. While the Φ_{ur}-pulse rotates by 180_x° in the pass-band, the Φ_{xyz}-pulse performs both $+180_x^\circ$ ($\Phi_{\text{ur}} = 0$) and -180_x° ($\Phi_{\text{ur}} = 1$) rotations for different off-resonance frequencies within the slice. The cost function Φ_{xyz} has high fidelity when the desired magnetization vector is created by a $+180_x^\circ$ or a -180_x° pulse. There is a transition zone between the regions with positive and negative rotation directions which does not perform a positive or negative 180_x° rotation. This

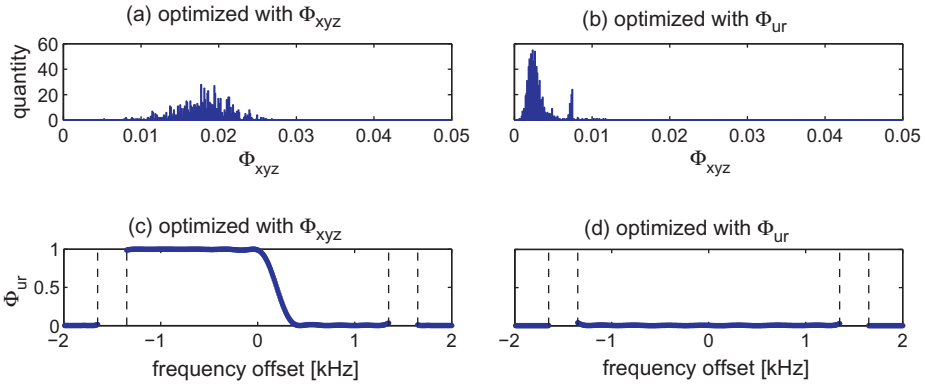

Fig. 1. Histograms of final cost Φ_{xyz} starting from 1000 initial pulses and optimizing with (a) Φ_{xyz} and (b) Φ_{ur}. (c and d) Cost depending on off-resonance frequency using the best pulse from (a) respectively (b). In the pass-band cost function Φ_{ur} was used, which is sensitive to the rotation direction. Dashed lines indicate the transition zone. (c) The pulse optimized with Φ_{xyz} contains different rotation directions within the slice. (d) The pulse optimized with Φ_{ur} performs well throughout the slice.

transition zone, which leads to poor fidelity under Φ_{xyz} as well as Φ_{ur}, can be avoided by using Φ_{ur}, which defines the rotation direction of the 180° pulse.

It is therefore very important to have a defined rotation direction for the pulse optimization. In practice, direct optimization of universal rotations with Φ_{ur} results in better performing 180° pulses, than optimization of point-to-point transformation of three orthogonal vectors with Φ_{xyz}.

3.2. Pulse shape symmetry

BB-SLR pulses have symmetric amplitude and anti-symmetric phase. This symmetry property was shown to be necessary in order to completely refocus the *x*-component of magnetization in crushed spin-echo [8]. In order to explore whether pulses with this symmetry property can be robust to B_1 variations we optimized pulses with and without symmetry constraints ($T \cdot BW = 15$, $BW/f_{1,max} = 3$, $FTW = 0.16$).

The symmetric pulses have similar pulse shape and similar behavior to B_1 scaling irrespective to optimization without B_1 robustness or with ±20% B_1 robustness (Fig. 2a and b). The pulse optimized without symmetry constraints shows good B_1 robustness (Fig. 2c). Therefore constraining pulse optimization to symmetric amplitude and anti-symmetric phase prevented the optimization of reaching good robustness against B_1 scaling. Subsequent pulses are optimized without symmetry constraints to obtain B_1 robustness.

3.3. Time-optimal curve

Time-optimal curves give a relationship for the achievable cost as a function of pulse duration. S-BURBOP pulses were optimized with different pulse durations and B_1 robustness using similar parameters as for the exemplary BB-SLR pulses described in Table 2. The parameters FTW and $BW/f_{1,max}$ were fixed for each time series of optimizations. All pulses are scaled to $B_{1,max} = 23$ μT which corresponds to $f_{1,max} = 1$ kHz for ^{1}H. Time-optimal curves were generated for the three cases of $BW/f_{1,max} = 1.88$, 2.36, and 2.83. For these three cases the results were qualitatively similar with respect to Φ vs. *T* and *E* vs. *T*. Therefore only the results for the largest bandwidth ($BW/f_{1,max} = 2.83$) are shown here. The resulting pulses are evaluated based on final cost and pulse energy (Fig. 3).

With increasing pulse duration *T* the cost Φ decreases and pulse energy increases. A decreasing cost means that ripple and FTW decrease. The conventional, purely amplitude-modulated, SLR pulse has a high cost because it is not broadband under the same $B_{1,max}$ limitation. It is included in order to have a relative measure of pulse energy.

Pulses optimized for exact B_1 calibration (S-BURBOP-0%) and for similar pulse duration reach a similar cost compared to BB-SLR (Fig. 3a). The advantage of S-BURBOP increases if the required B_1 robustness increases. S-BURBOP-10% and S-BURBOP-20% are optimized for a B_1 miscalibration of ±10% and ±20%, respectively. S-BURBOP-10% with $T = 6$ ms has only 25% of the cost (including the different B_1 scalings) of BB-SLR (Fig. 3b). For S-BURBOP-20% the cost decreases to only 20% of BB-SLR (Fig. 3c).

Instead of reducing cost (i.e. increasing performance) with a pulse of similar duration the time-optimal curve also facilitates selecting a pulse of similar cost and shorter pulse duration. For ±10% B_1 robustness this means that compared to BB-SLR the same cost can be reached with a pulse duration shortened by 45% and energy reduced by 34%. For S-BURBOP-20% the pulse duration can be reduced by 58% and energy by 48% while obtaining the same cost. Hence, echo time and energy can be significantly reduced with S-BURBOP-10% and S-BURBOP-20%, if robustness against B_1 scaling is needed.

Besides reducing pulse duration time-optimal curves can also be used to reduce energy while obtaining the same cost as a reference pulse (e.g. BB-SLR). The iterative optimization used here can limit pulse energy which results in a tradeoff between pulse performance and pulse energy [22,34].

3.4. Performance of exemplary pulses

Three exemplary S-BURBOP-20% pulses are selected for further comparison to BB-SLR. The exemplary pulses are chosen to be similar to the exemplary BB-SLR pulses from Ref. [8]. The pulse properties are described in Table 2 and the shape of the pulse with the largest bandwidth is shown in Fig. 4a.

Compared to the corresponding BB-SLR pulses the S-BURBOP-20% reach slightly larger $T \cdot BW$, similar $BW/f_{1,max}$, smaller FTW, and slightly larger *E*. The ripples for exact B_1 calibration are larger. The pass-band and stop-band ripples for exact B_1 are increased by a factor of 2–3 and 218–490, respectively. However, the ripples remain in a range where they are practically applicable. In Table 2 the ripples are also compared for B_1 scaling. For B_1 scaling of ±20% BB-SLR pulses become practically unusable, as the pass-band ripple becomes too large (often larger than 100%). This means that the rotation angle is far from the intended 180°, leading to signal cancelation. The ripples for S-BURBOP-20% are increased for ±20% B_1 scaling compared to exact B_1 , but remain much smaller than for BB-SLR.

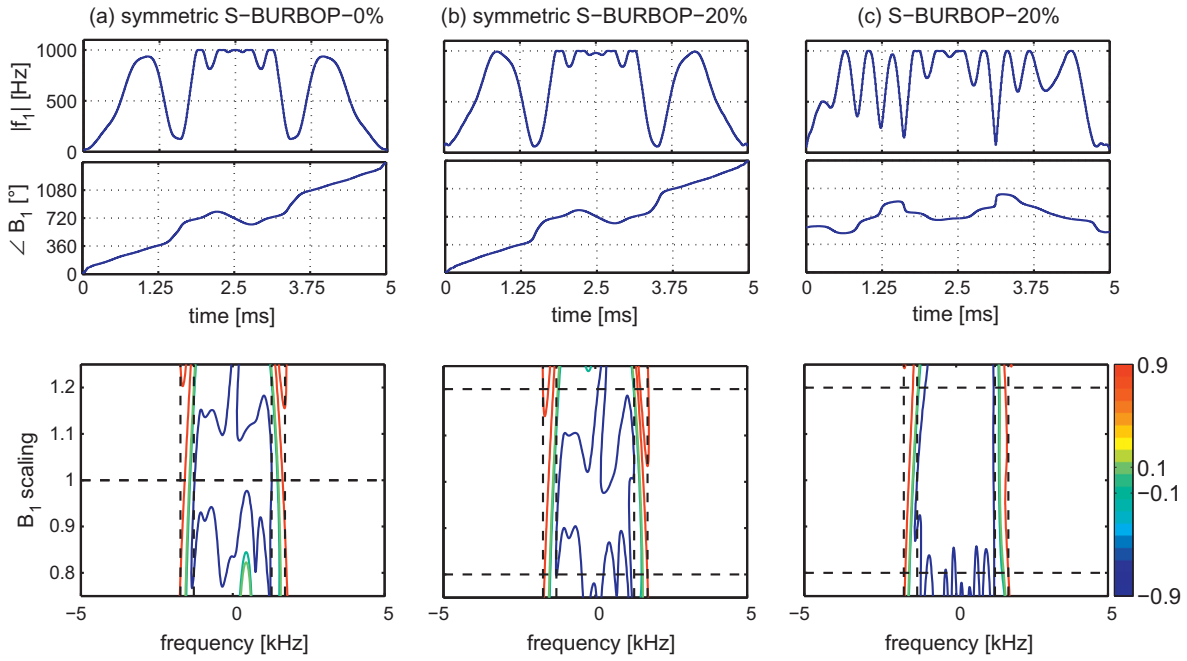

Fig. 2. Pulse shape and inverted z-magnetization of (a) symmetric S-BURBOP-0%, (b) symmetric S-BURBOP-20%, and (c) S-BURBOP-20% without symmetry constraints. S-BURBOP-0% was optimized without B1 robustness, while S-BURBOP-20% was optimized for ±20% B1 robustness. The symmetric pulses were optimized with time-symmetric amplitude and anti-symmetric phase. Symmetric S-BURBOP-0% and symmetric S-BURBOP-20% have similar pulse shape and B_1 robustness behavior. S-BURBOP-20% without this symmetry restriction shows good B_1 robustness.

Table 2
Properties of the exemplary pulses for a scaling of $f_{1,max}$ = 1 kHz. Energy E is normalized to the energy of the SLR pulse with the same $B_{1,max}$. The parameters BW and FTW are evaluated for exact B_1 scaling only. Maximum ripples in pass-band δ_{PB} and stop-band δ_{SB} are evaluated for exact B_1 and ±20% scaling.

	$T \cdot BW$	$BW/f_{1,max}$	FTW	E/E_{SLR}	T (ms)	BW (Hz)	$\delta_{PB} \cdot 100$ for B_1 scaling of			$\delta_{SB} \cdot 100$ for B_1 scaling of		
							−20%	0%	+20%	−20%	0%	+20%
SLR	4.10	0.97	0.42	1.00	4.21	974	22.73	1.06	21.43	3.14	1.20	22.63
BB-SLR	7.17	1.88	0.44	3.19	3.82	1876	>100	1.52	>100	0.31	0.001	3.62
S-BURBOP-20%	9.27	2.06	0.28	5.35	4.50	2061	28.55	4.15	5.69	0.22	0.49	2.54
BB-SLR	12.75	2.36	0.25	6.17	5.39	2364	>100	1.50	30.94	0.24	0.002	2.62
S-BURBOP-20%	13.84	2.52	0.22	6.30	5.50	2517	9.97	4.33	1.61	0.76	0.86	14.13
BB-SLR	16.73	2.83	0.18	6.92	5.91	2830	>100	1.57	>100	0.77	0.005	5.73
S-BURBOP-20%	19.49	3.00	0.16	7.51	6.50	2999	9.14	3.02	3.14	2.30	1.09	6.08
HS1	38.95	3.00	0.22	5.96	13.00	2996	17.77	4.53	2.07	0.69	0.83	0.83

Broad bandwidth and B_1 robustness can also be obtained with adiabatic pulses. A hyperbolic secant pulse (HS1) with $BW/f_{1,max} = 3$ and $T = 6.5$ ms was designed with a truncation factor $\beta = 5$ [14]. In order to achieve refocusing the HS1 pulse needs to be applied twice. The resulting pulse performance is given in Table 2. Compared to BB-SLR and S-BURBOP-20% with the same $BW/f_{1,max}$ the HS1 pulse has roughly twice the $T \cdot BW$, a larger FTW, and less energy. Pass-band ripples of HS1 are very large for B_1 scaling to 80% because the adiabatic condition is not fulfilled. In the other cases the performance with respect to ripples is comparable to S-BURBOP-20%. HS1 pulses may be applicable when short echo times are not necessary. S-BURBOP-20% pulses show a good magnetization profile for B_1 scaling within ±20% and are much shorter. They are very useful for common experiments with a volume resonator, where the B_1 inhomogeneity is within a limited range. Furthermore, if errors in the calibration of the B_1 amplitude exist, they are also within a small range.

The magnetization profile for inversion and crushed spin-echo (Fig. 4b and c) shows that the pulse performs within the specifications of slice and transition zone. The pass-band and stop-band errors for inversion and for exact B_1 calibration are 0.03 and 0.01, respectively. These ripples are small enough for practical experiments. For crushed spin-echo there remains x-magnetization as S-BURBOP-20% pulses do not have symmetric amplitude and anti-symmetric phase (Fig. 4c). The remaining x-magnetization integrated over all frequencies is zero and the phase error remains very small within the pass-band.

Robustness against B_1 scaling can best be judged from contour plots (Fig. 5), which show magnetization after applying the pulses as inversion and crushed spin-echo pulses depending on resonance offset and B_1 scaling. The exemplary pulse inverts z-magnetization to below −0.9 within the slice specifications and for B_1 scaling between 0.79 and ≈1.2. For crushed spin-echo a performance better than −0.9 is achieved for B_1 scalings within 0.78 to ≈1.2. For the corresponding BB-SLR pulse these B_1 scalings are 0.98–1.02 for inversion and 0.96–1.05 for crushed spin-echo. Compared to the BB-SLR pulse the robustness against B_1 errors is highly improved, while staying within the slice specifications. Magnetization profiles of spin-echo experiments corresponded well to simulations and confirmed these findings (Fig. 6).

3.5. Experimental validation

The applicability of S-BURBOP-20% pulses was shown in PRESS CSI experiments in a phantom filled with oil and water (Fig. 7). The 3.5 ppm chemical-shift difference between oil and water results in

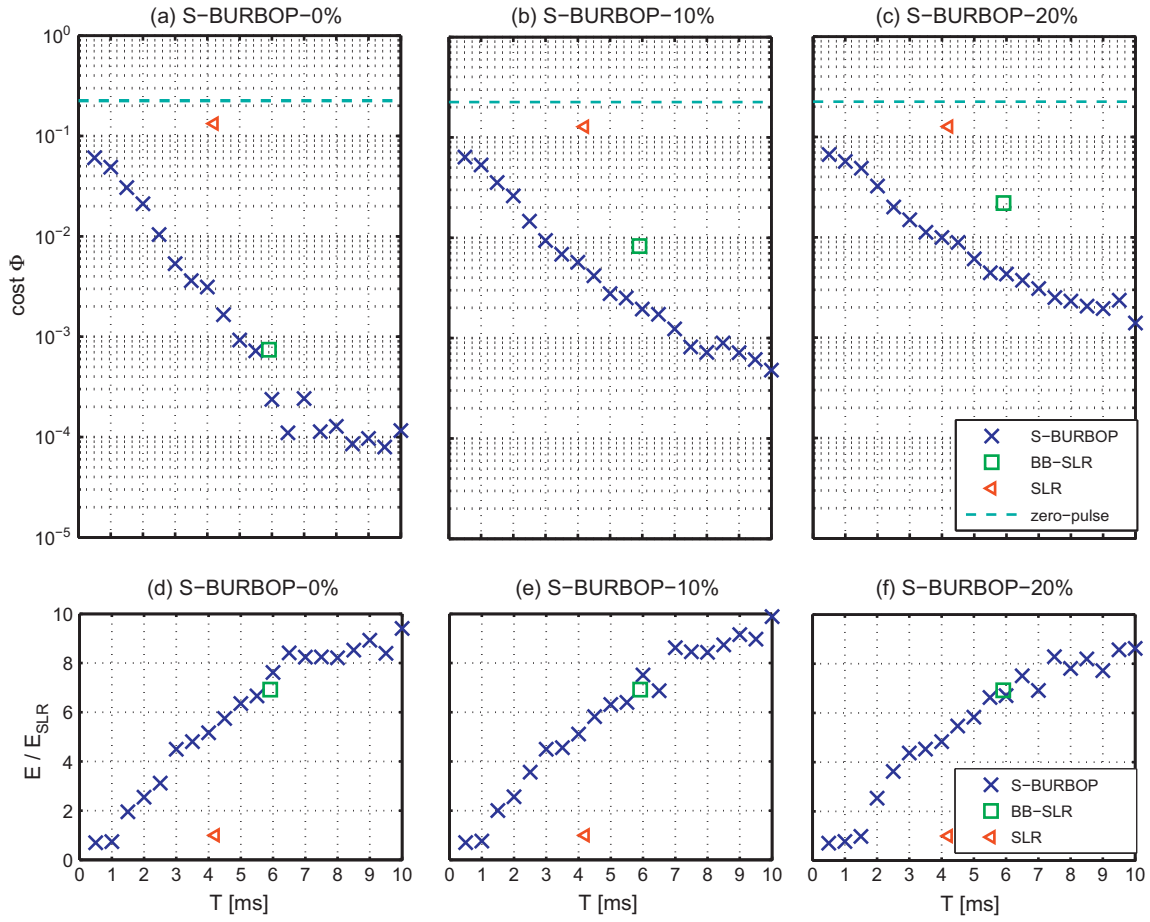

Fig. 3. (a–c) Final cost for S-BURBOP pulses with different duration optimized for B_1 inhomogeneity of (a) ±0%, (b) ±10 %, and (c) ±20%. SLR and BB-SLR are included for comparison. The cost for a pulse of zero amplitude (dashed line) is smaller than unity since it performs perfectly in the stop-band, which contributes positively to the cost measure. (d–f) Pulse energy normalized to SLR pulse for the above pulses.

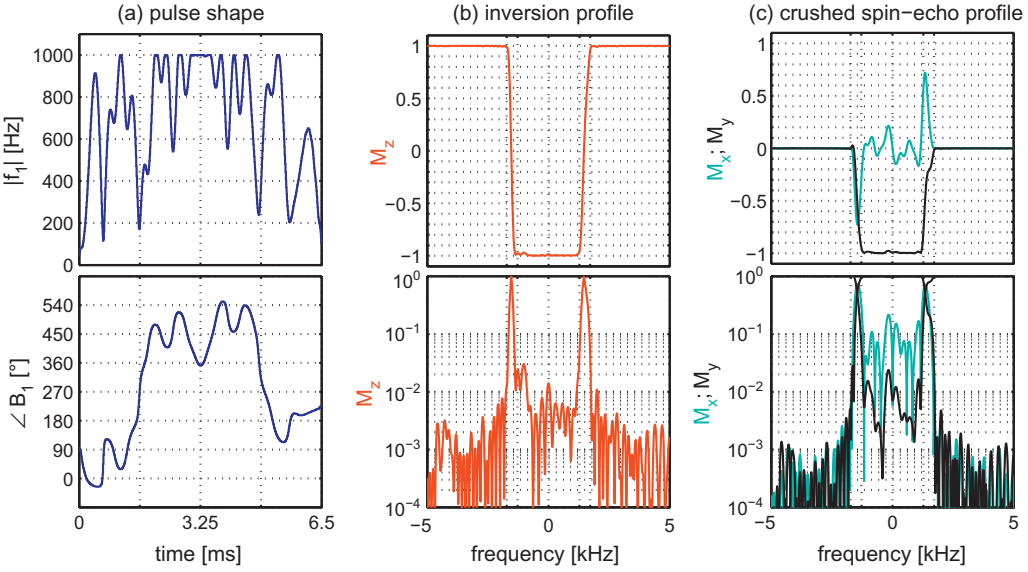

Fig. 4. (a) RF pulse amplitude and phase for exemplary S-BURBOP-20% with $BW/f_{1,max} = 3$. (b) Magnetization profile after application of exemplary S-BURBOP-20% as inversion and (c) crushed spin-echo pulse. Bottom profiles in logarithmic scale show the magnetization errors. The profile was simulated for exact calibration of $B_1 = 23$ μT.

a chemical-shift displacement error (CSDE) of 36% of slice thickness for the SLR pulse. With the broadband pulses BB-SLR and S-BURBOP-20% the CSDE is reduced to 10% and the selection is sharper (see magnetization profiles in Fig. 7k). This means that the width of the transition zone is reduced, leading to less sensitivity toward anomalous J-modulation and reducing the need for outer volume suppression.

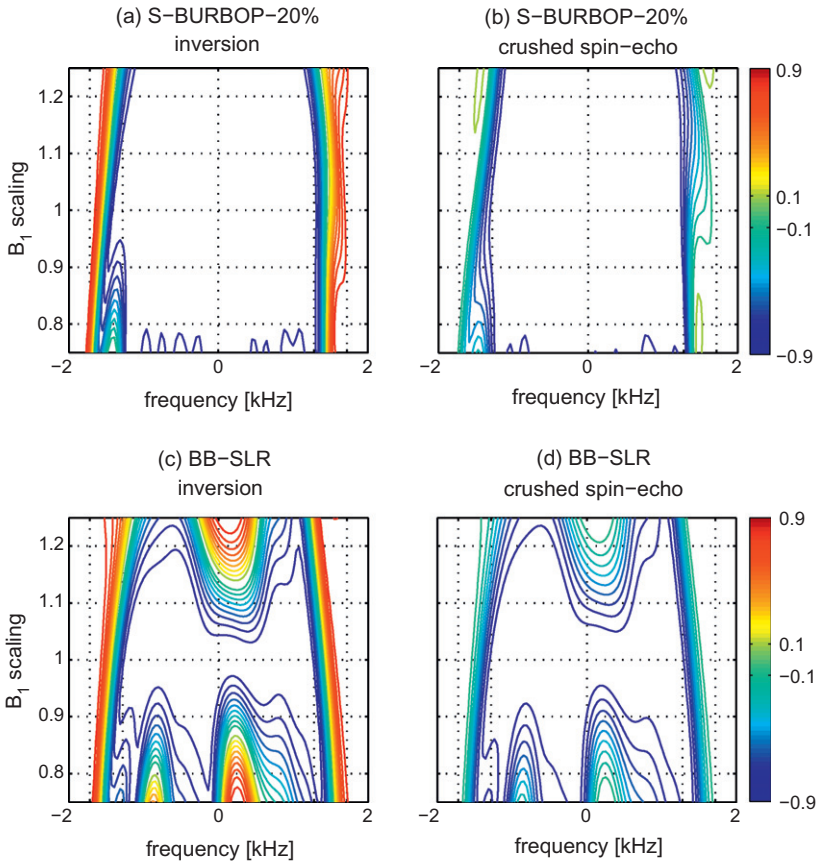

Fig. 5. Simulated contour plot of magnetization after using the exemplary S-BURBOP-20% shown in Fig. 4a as (a) inversion and (b) crushed spin-echo pulse. The plots show pulse behavior depending on different resonance offsets and B_1 scalings. (c and d) Show the same simulations for a comparable BB-SLR pulse. Robustness against B_1 scaling is highly improved with S-BURBOP-20%.

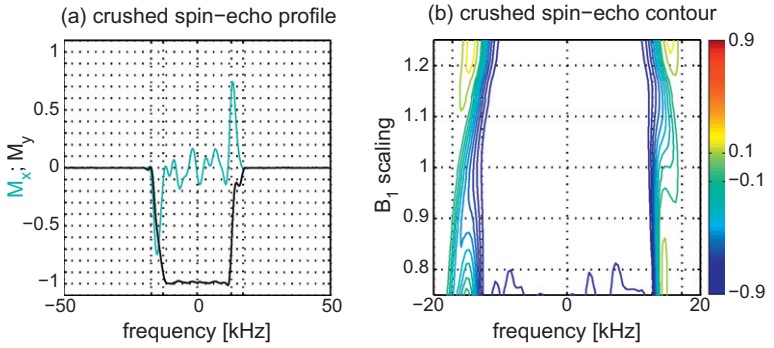

Fig. 6. Magnetization profile from crushed spin-echo experiment using S-BURBOP-20% shown in Fig. 4a. (a) The profile shows x- and y-magnetization for exact B_1 calibration. (b) The contour plot shows y-magnetization for ±25% B_1 scaling. Note that the experiments were performed with a 10-fold B_1 amplitude compared to the simulations, which results in a 10-fold bandwidth.

Furthermore, PRESS experiments were performed with a miscalibrated B_1 amplitude. For 80% of correct B_1 the SLR and S-BURBOP-20% pulses show only a minor increase in ripples, while the BB-SLR pulse causes a large drop in signal (Fig. 7 (left column)). For BB-SLR the selection of the desired voxel is incomplete, leading to signal cancellation in some areas. For 120% B_1 (Fig. 7 (right column)) the signal drop is equally severe for BB-SLR. With SLR the selection was moderate, showing large ripples in the stop-band and smaller signal amplitude of water. The S-BURBOP-20% pulse showed good selection and a larger water signal than with the SLR pulse. In the exemplary slice profile S-BURBOP-20% obtained more than 86% of signal for ±20% B_1 errors.

The SLR pulse is fairly robust against B_1 miscalibration but results in a large CSDE. BB-SLR reduces the CSDE successfully, but is highly sensitive to B_1 errors. S-BURBOP-20% effectively reduced the CSDE while being robust toward B_1 scaling of ±20%.

4. Conclusion

Refocusing pulses which are robust, highly selective, and broadband were designed using optimal control theory. In simulations and experiments these S-BURBOP-20% pulses were shown to fulfill broadband slice specifications over a range of ±20% B_1 scaling. S-BURBOP-20% pulses have experimental advantages due to their

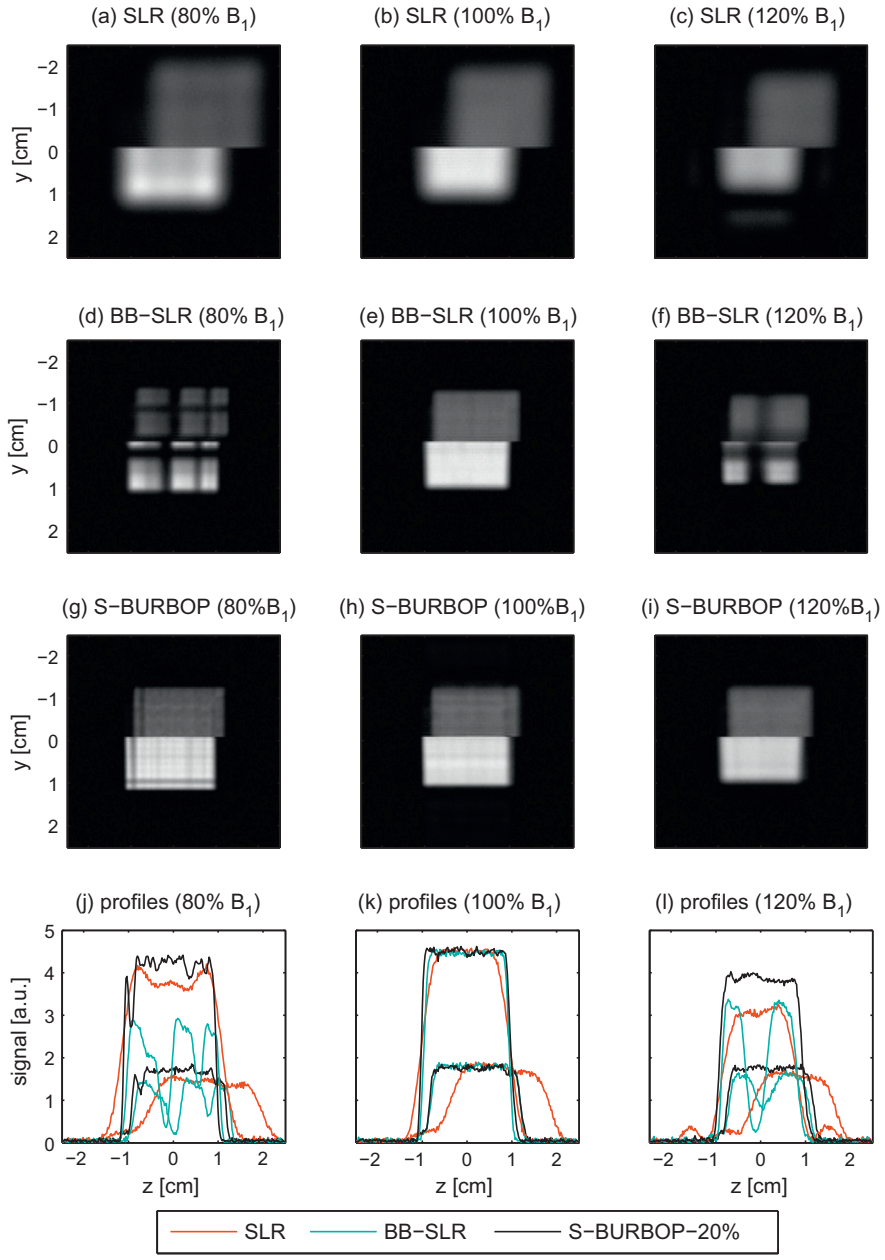

Fig. 7. Voxel from PRESS CSI experiments in a phantom filled with water and oil using (a–c) SLR, (d–f) BB-SLR, and (g–i) S-BURBOP-20% refocusing pulses. Plots (j–l) show horizontal profiles from the above images through water (y = 1 cm) and oil (y = −1 cm). In the center column B_1 was calibrated correctly, while in the left and right columns B_1 was scaled by -20% and +20%, respectively. The chemical shift displacement error between signals from oil and water is reduced with larger bandwidth. S-BURBOP-20% was shown to be robust against B_1 scaling of ±20%. The pulses had a $BW/f_{1,\max}$ = 0.97, 2.83, 3.00, respectively.

robust behavior toward B_1 scaling, whereas broadband SLR pulses showed high B_1 sensitivity. Compared to hyperbolic-secant (HS1) pulses S-BURBOP-20% pulses allow a much shorter echo time because they are universal rotation pulses and do not need to be used in pairs. The broadband property of S-BURBOP-20% pulses leads to a reduction of chemical-shift displacement errors (CSDE). In PRESS experiments the CSDE between fat and water was reduced by a factor of 3 compared to a conventional SLR pulse.

Acknowledgements

We gratefully acknowledge support from Dr. Kyryl Kobzar and Dr. Ralph Noeske. This work was partially funded by Bundesministerium für Bildung und Forschung MOBITUM grants 01EZ0826/01EZ0827, and the Faculty Graduate Center Chemistry at Technische Universität München.

Appendix A. Relationships between Φ_{ur}, Φ_{ur2}, and Φ_{xyz}

Following is the proof showing that the cost function Φ_{xyz} (Eq. (22)) is identical to Φ_{ur2} (Eq. (21)). Inserting initial magnetization vectors

$$\vec{M}_{0,1} = \begin{bmatrix} 1 \\ 0 \\ 0 \end{bmatrix}, \quad \vec{M}_{0,2} = \begin{bmatrix} 0 \\ 1 \\ 0 \end{bmatrix}, \quad \vec{M}_{0,3} = \begin{bmatrix} 0 \\ 0 \\ 1 \end{bmatrix}, \tag{29}$$

target magnetization vectors (Eq. (23)), and Φ_{pp} (Eq. (7)) into Φ_{xyz} gives

$$\Phi_{xyz} = 0.75 - 0.25[(R_t\vec{M}_{0,1})^T R\vec{M}_{0,1} + (R_t\vec{M}_{0,2})^T R\vec{M}_{0,2} + (R_t\vec{M}_{0,3})^T R\vec{M}_{0,3}]. \quad (30)$$

The rotation matrix $R = R_N \cdots R_1$ describes the rotation of the RF pulse sequence by the angle ϕ around the axis $\vec{n}$. It is given by [35]

$$R = \begin{bmatrix} \cos\phi + n_x^2(1-\cos\phi) & n_x n_y(1-\cos\phi) - n_z\sin\phi & n_x n_z(1-\cos\phi) + n_y\sin\phi \\ n_y n_x(1-\cos\phi) + n_z\sin\phi & \cos\phi + n_y^2(1-\cos\phi) & n_y n_z(1-\cos\phi) - n_x\sin\phi \\ n_z n_x(1-\cos\phi) - n_y\sin\phi & n_z n_y(1-\cos\phi) + n_x\sin\phi & \cos\phi + n_z^2(1-\cos\phi) \end{bmatrix} \quad (31)$$

With the norms $|\vec{n}| = |\vec{n}_t| = 1$ and the substitution $A = n_{x,t}n_x + n_{y,t}n_y + n_{z,t}n_z$, Eq. (30) becomes

$$\Phi_{xyz} = 0.75 - 0.25[(1+A^2)\cos\phi_t\cos\phi + (1-A^2)\cos\phi_t + (1-A^2)\cos\phi + A^2 + 2A\sin\phi_t\sin\phi] \quad (32)$$

On the other hand, the cost function Φ_{ur2}, which compared to Φ_{ur} (Eq. (16)) contains the squared value of $\mathrm{tr}\{Q_t^\dagger \cdot Q\}$, is given by

$$\Phi_{ur2} = 1 - \left(\cos\frac{\phi_t}{2}\cos\frac{\phi}{2} + A\sin\frac{\phi_t}{2}\sin\frac{\phi}{2}\right)^2 \quad (33)$$

With the help of $\cos^2 x = 0.5 + 0.5\cos(2x)$; $\sin^2 x = 0.5 - 0.5\cos(2x)$ and $\sin x \cdot \cos x = 0.5\sin(2x)$ this equation transforms into

$$\begin{aligned}\Phi_{ur2} &= 1 - 0.25\,[(1+A^2)\cos\phi_t\cos\phi + (1-A^2)\cos\phi_t \\ &\quad + (1-A^2)\cos\phi + 1 + A^2 + 2A\sin\phi_t\sin\phi] \\ &= 0.75 - 0.25\,[(1+A^2)\cos\phi_t\cos\phi + (1-A^2)\cos\phi_t \\ &\quad + (1-A^2)\cos\phi + A^2 + 2A\sin\phi_t\sin\phi] \end{aligned} \quad (34)$$

which is equal to Eq. (32). This proofs the identity $\Phi_{xyz} = \Phi_{ur2}$.

If a cost function has a 2π-periodicity it is impossible to distinguish π rotations around the x vs. $-x$ axis (or π vs. $-\pi$ rotations around the x axis). From Eq. (34) it can be seen that Φ_{ur2} is invariant to 2π shifts: $\Phi_{ur2}(\phi - 2\pi) = \Phi_{ur2}(\phi)$, because the sine and cosine functions are symmetric to 2π shifts. Conversely, Φ_{ur} is not periodic to 2π shifts:

$$\begin{aligned}\Phi_{ur}(\phi - 2\pi) &= 0.5 - 0.25\left(2\left[\cos\frac{\phi_t}{2}\cos\frac{\phi-2\pi}{2} + A\sin\frac{\phi_t}{2}\sin\frac{\phi-2\pi}{2}\right]\right) \\ &= 0.5 + 0.25\left(2\left[\cos\frac{\phi_t}{2}\cos\frac{\phi}{2} + A\sin\frac{\phi_t}{2}\sin\frac{\phi}{2}\right]\right) \neq \Phi_{ur}(\phi) \\ &= 0.5 - 0.25\left(2\left[\cos\frac{\phi_t}{2}\cos\frac{\phi}{2} + A\sin\frac{\phi_t}{2}\sin\frac{\phi}{2}\right]\right) \end{aligned} \quad (35)$$

Therefore Φ_{ur} distinguishes π from $-\pi$ rotations, as expected.

References

[1] B. Ross, S. Bluml, Magnetic resonance spectroscopy of the human brain, Anat. Rec. 265 (2) (2001) 54–84.
[2] P.A. Bottomley, Spatial localization in NMR spectroscopy in vivo, Ann. NY Acad. Sci. 508 (1987) 333–348.
[3] T.R. Brown, B.M. Kincaid, K. Ugurbil, NMR chemical shift imaging in three dimensions, Proc. Natl. Acad. Sci. USA 79 (11) (1982) 3523–3526.
[4] D.A. Yablonskiy, J.J. Neil, M.E. Raichle, J.J. Ackerman, Homonuclear J coupling effects in volume localized NMR spectroscopy: pitfalls and solutions, Magn. Reson. Med. 39 (2) (1998) 169–178.
[5] R.A. Edden, P.B. Barker, If J doesn't evolve, it won't J-resolve: J-PRESS with bandwidth-limited refocusing pulses, Magn. Reson. Med. 65 (2011) 1509–1514.
[6] S. Conolly, D. Nishimura, A. Macovski, Optimal control solutions to the magnetic resonance selective excitation problem, IEEE Trans. Med. Imaging 5 (2) (1986) 106–115.
[7] J. Pauly, P.L. Roux, D. Nishimura, A. Macovski, Parameter relations for the Shinnar-Le Roux selective excitation pulse design algorithm, IEEE Trans. Med. Imaging 10 (1) (1991) 53–65.
[8] R.F. Schulte, P.L. Roux, M.W. Vogel, H. Koenig, Design of phase-modulated broadband refocusing pulses, J. Magn. Reson. 190 (2) (2008) 271–279.
[9] B. Luy, K. Kobzar, T.E. Skinner, N. Khaneja, S.J. Glaser, Construction of universal rotations from point-to-point transformations, J. Magn. Reson. 176 (2) (2005) 179–186.
[10] T. Raidy, N. Sailasuta, R. Hurd, J. Pauly, Application of reduced flip angle "180°" RF pulses in PRESS, in: 3rd Annual Meeting of the International Society of Magnetic Resonance in Medicine, Nice, 1995, p. 1020.
[11] S. Pickup, X. Ding, Pulses with fixed magnitude and variable phase response profiles, Magn. Reson. Med. 33 (5) (1995) 648–655.
[12] S. Pickup, M. Popescu, Efficient design of pulses with trapezoidal magnitude and linear phase response profiles, Magn. Reson. Med. 38 (1) (1997) 137–145.
[13] S. Conolly, G. Glover, D. Nishimura, A. Macovski, A reduced power selective adiabatic spin-echo pulse sequence, Magn. Reson. Med. 18 (1) (1991) 28–38.
[14] M. Garwood, L. DelaBarre, The return of the frequency sweep: designing adiabatic pulses for contemporary NMR, J. Magn. Reson. 153 (2) (2001) 155–177.
[15] J. Mao, T. Mareci, K. Scott, E. Andrew, Selective inversion radiofrequency pulses by optimal control, J. Magn. Reson. 70 (1986) 310–318.
[16] K. Kobzar, B. Luy, N. Khaneja, S.J. Glaser, Pattern pulses: design of arbitrary excitation profiles as a function of pulse amplitude and offset, J. Magn. Reson. 173 (2) (2005) 229–235.
[17] G.B. Matson, K. Young, L.G. Kaiser, RF pulses for in vivo spectroscopy at high field designed under conditions of limited power using optimal control, J. Magn. Reson. 199 (1) (2009) 30–40.
[18] T.E. Skinner, T.O. Reiss, B. Luy, N. Khaneja, S.J. Glaser, Application of optimal control theory to the design of broadband excitation pulses for high-resolution NMR, J. Magn. Reson. 163 (1) (2003) 8–15.
[19] K. Kobzar, T.E. Skinner, N. Khaneja, S.J. Glaser, B. Luy, Exploring the limits of broadband excitation and inversion pulses, J. Magn. Reson. 170 (2) (2004) 236–243.
[20] T.E. Skinner, K. Kobzar, B. Luy, M.R. Bendall, W. Bermel, N. Khaneja, S.J. Glaser, Optimal control design of constant amplitude phase-modulated pulses: application to calibration-free broadband excitation, J. Magn. Reson. 179 (2) (2006) 241–249.
[21] N.I. Gershenzon, K. Kobzar, B. Luy, S.J. Glaser, T.E. Skinner, Optimal control design of excitation pulses that accommodate relaxation, J. Magn. Reson. 188 (2) (2007) 330–336.
[22] K. Kobzar, T.E. Skinner, N. Khaneja, S.J. Glaser, B. Luy, Exploring the limits of broadband excitation and inversion: II. RF-power optimized pulses, J. Magn. Reson. 194 (1) (2008) 58–66.
[23] N. Khaneja, T. Reiss, C. Kehlet, T. Schulte-Herbrüggen, S.J. Glaser, Optimal control of coupled spin dynamics: design of NMR pulse sequences by gradient ascent algorithms, J. Magn. Reson. 172 (2) (2005) 296–305.
[24] J.L. Neves, B. Heitmann, T.O. Reiss, H.H.R. Schor, N. Khaneja, S.J. Glaser, Exploring the limits of polarization transfer efficiency in homonuclear three spin systems, J. Magn. Reson. 181 (1) (2006) 126–134.
[25] Z. Tosner, T. Vosegaard, C. Kehlet, N. Khaneja, S.J. Glaser, N.C. Nielsen, Optimal control in NMR spectroscopy: numerical implementation in SIMPSON, J. Magn. Reson. 197 (2) (2009) 120–134.
[26] N.C. Nielsen, C. Kehlet, S.J. Glaser, N. Khaneja, Optimal control methods in NMR spectroscopy, Encyclopedia Nucl. Magn. Reson. (2010). doi:10.1002/9780470034590.emrstm1043.
[27] K. Kobzar, Optimal Control, Partial Alignment and More: The Design of Novel Tools for NMR Spectroscopy of Small Molecules, Ph.D. Thesis, Technische Universität München, 2007.
[28] T.W. Borneman, M.D. Hürlimann, D.G. Cory, Application of optimal control to CPMG refocusing pulse design, J. Magn. Reson. 207 (2) (2010) 220–233.
[29] A.E. Bryson, Applied Optimal Control, Wiley, New York, 1975.
[30] L. Emsley, G. Bodenhausen, Optimization of shaped selective pulses for NMR using a quaternion description of their overall propagators, J. Magn. Reson. 97 (1992) 135–148.
[31] W.S. Warren, Effects of arbitrary laser or NMR pulse shapes on population inversion and coherence, J. Chem. Phys. 81 (1984) 5437.
[32] A. Walther, B. Julsgaard, L. Rippe, Y. Ying, S. Kröll, R. Fisher, S. Glaser, Extracting high fidelity quantum computer hardware from random systems, Phys. Scr. T137 (2009) 014009. doi:10.1088/0031-8949/2009/T137/014009.
[33] T. Schulte-Herbrüggen, A. Spörl, N. Khaneja, S.J. Glaser, Optimal control-based efficient synthesis of building blocks of quantum algorithms: A perspective from network complexity towards time complexity, Phys. Rev. A 72 (2005) 042331.
[34] M.A. Janich, R.F. Schulte, M. Schwaiger, S.J. Glaser, Broadband refocusing pulses with B_1 robustness and energy constraints, in: 19th Annual Meeting & Exhibition of the International Society of Magnetic Resonance in Medicine, Montreal, 2011, p. 2913.
[35] H. Goldstein, Classical mechanics, Addison-Wesley Publishing Company, 1980.